JACS
JOURNAL OF THE AMERICAN CHEMICAL SOCIETY

Article

pubs.acs.org/JACS

Surface Charge Visualization at Viable Living Cells

David Perry,[†,‡] Binoy Paulose Nadappuram,[†] Dmitry Momotenko,[†] Philip D. Voyias,[§] Ashley Page,[†,‡] Gyanendra Tripathi,[§] Bruno G. Frenguelli,[∥] and Patrick R. Unwin*[,†]

[†]Department of Chemistry, [‡]MOAC Doctoral Training Centre, [§]Division of Metabolic and Vascular Health, Warwick Medical School, and [∥]School of Life Sciences, University of Warwick, Coventry CV4 7AL, United Kingdom

Supporting Information

ABSTRACT: Scanning ion conductance microscopy (SICM) is demonstrated to be a powerful technique for quantitative nanoscale surface charge mapping of living cells. Utilizing a bias modulated (BM) scheme, in which the potential between a quasi-reference counter electrode (QRCE) in an electrolyte-filled nanopipette and a QRCE in bulk solution is modulated, it is shown that both the cell topography and the surface charge present at cellular interfaces can be measured simultaneously at high spatial resolution with dynamic potential measurements. Surface charge is elucidated by probing the properties of the diffuse double layer (DDL) at the cellular interface, and the technique is sensitive at both low-ionic strength and under typical physiological (high-ionic strength) conditions. The combination of experiments that incorporate pixel-level self-referencing (calibration) with a robust theoretical model allows for the analysis of local surface charge variations across cellular interfaces, as demonstrated on two important living systems. First, charge mapping at *Zea mays* root hairs shows that there is a high negative surface charge at the tip of the cell. Second, it is shown that there are distinct surface charge distributions across the surface of human adipocyte cells, whose role is the storage and regulation of lipids in mammalian systems. These are new features, not previously recognized, and their implications for the functioning of these cells are highlighted.

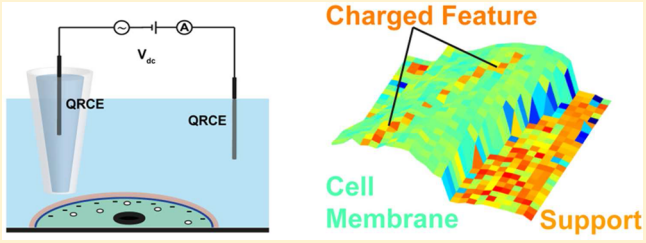

INTRODUCTION

Surface charge is known to play a key role in a host of different dynamic interfacial processes and equilibria,[1] from the stability of colloids[2,3] and crystal growth/dissolution[4,5] to nanoscale analytical devices[6−8] and biological systems, where it determines structure and function at levels ranging from biomolecular assemblies[9] to complex life forms such as living cells and organisms.[10−13] Interfacial charge is thought to influence cellular communication,[14−16] cell adherence to surfaces,[17−19] uptake of nutrients,[20] molecules and particles,[21−24] and cell growth and division,[25,26] among other processes. The ability to visualize local surface charge, and also to identify charge heterogeneities on living cell surfaces, would thus be hugely beneficial in unraveling fundamental questions of cell function.

Probing surface charge, however, remains a difficult task owing to a lack of robust techniques capable of measurements at the micro- and nanoscale in complex (relevant) environments. This is particularly the case for studies of living systems, where physiological conditions are usually required to maintain cell viability. Typically, physiological media require aqueous electrolyte solutions of high-ionic strength (∼150 mM), and under these conditions the diffuse double layer (DDL) is compressed to a subnanometer scale.[27,28] In such cases, mapping surface charges by probing the DDL around viable cells become troublesome, since the surface charge is well screened by electrolyte ions. This difficulty is compounded by the fact that living cells are intrinsically soft, fragile, and sensitive to external perturbation/stimulation. While atomic force microscopy (AFM) has been used extensively for mapping the surface properties of living cells,[29−33] as well as being used for the study of double layer characteristics of inert and living systems,[34−40] AFM force−distance curves are not easily analyzed because various forces can act on the probe.[41,42] Moreover, at high-electrolyte concentrations (physiological conditions), the tip−substrate distance over which AFM becomes sensitive to surface charge becomes extremely compressed to a nm, or less, making charge measurements particularly challenging.

In this paper we describe how the surface charge at living cells can be imaged, probed, and analyzed through the use of local ion-conductance measurements. Scanning ion conductance microscopy (SICM),[27,43−46] involves the use of a nanopipette filled with electrolyte positioned above a substrate that is also bathed in electrolyte. A potential is typically applied between a quasi-reference counter electrode (QRCE) in the nanopipette and one in bulk solution to generate an ionic current.[47,48] Changes in resistance as the probe approaches an interface (sample) allow the ionic current to be used for positional feedback for high-resolution topographical imaging.[43,44,49,50] For improved stability, a vertical oscillation of pipette position[51] or bias modulation[52] (BM) is applied to

Received: December 16, 2015
Published: February 12, 2016

DOI: 10.1021/jacs.5b13153
J. Am. Chem. Soc. 2016, 138, 3152−3160

generate alternating components of the ionic current (AC) as the feedback signal.

The capabilities of SICM have recently been expanded to embrace the imaging and probing of charge distributions on a variety of model substrates semiquantitatively via surface induced rectification (SIR) of the ion current.[53−56] SICM does not probe the surface charge itself, but the ionic atmosphere around a charged interface,[52] making the technique less invasive compared to other methods (e.g., AFM), which is desirable for the study of living cells in their natural state. Herein, using a combination of BM-SICM and finite element method (FEM) simulations, we demonstrate that even in solutions of high salt concentration (ionic strength 150 mM) it is possible to quantify simultaneously the surface charge at living cells and cell topography, as well as to identify heterogeneously distributed features across cellular membrane surfaces. Our studies are exemplified through studies of: *Zea mays* (common corn) root hair cells at low-electrolyte concentrations, where knowledge of cell charge would aid in understanding the absorption mechanisms important in this system,[57] and human adipocytes under physiological conditions, where the cell surface charge plays a great role in cell uptake properties.[58]

MATERIALS AND METHODS

Solutions. Milli-Q reagent grade water (resistivity ca. 18.2 MΩ cm at 25 °C) was used for all solutions. 10 mM KCl (Sigma-Aldrich) solution was prepared and used for the SICM experiments involving root hair cells. Preadipocyte cells were grown to confluence in Dulbecco's modified eagle medium (DMEM)/Ham's F-12 phenol-free medium (Invitrogen, U.K.) containing 10% FCS, penicillin (100 U/mL), streptomycin (100 μg/mL), and transferrin (5 μg/mL). Differentiation media (Promocell, Germany) for the preadipocytes contained biotin (8 μg/mL), insulin (500 ng/mL), dexamethasone (400 ng/mL), 3-isobutyl-1-methylxanthine (IBMX, 44 μg/mL), L-thyroxin (9 ng/mL), and ciglitazone (3 μg/mL). The adipocytes were then grown in nutrition media (NM) containing DMEM/Ham's F-12, 3% FCS, D-biotin (8 μg/mL), insulin (500 ng/mL), and dexamethasone (400 ng/mL). Adipocyte cells were imaged in DMEM/F-12 media (Invitrogen) containing one adipocyte nutrition medium supplement pack (Promocell).

Cell Culturing and Preparation. Human abdominal subcutaneous (AbSc) adipose tissue (AT) was digested with collagenase to isolate preadipocytes, which were cultured in tissue culture flasks until confluent and then trypsinized to obtain cells used in this work. The preadipocytes from the same passage were then grown to confluence in the above-specified growth media. At confluence, preadipocytes were differentiated in differentiation media for 72 h. After this period, the differentiating cells were grown in nutrition media until fully differentiated (14−18 days), and the viability of adipocytes was assessed using the trypan blue dye exclusion method[59] (Sigma−Aldrich).

Zea mays seeds (Avenir, Syngenta) were germinated between two layers of damp paper at 25 °C for 4 days. This provided a root of approximately 20 mm in length with a dense layer of root hair cells. At this stage of development, all nutrients for the corn growth are still provided by the seed.

Imaging Substrates. AbSc cells were adhered to a collagen-coated Petri dish in order to keep them stationary for imaging purposes without impacting their viability. The corn roots were attached away from the point of imaging to a glass bottomed Petri dish (3512, WillcoWells) using SPM adhesive tabs (Agar Scientific).

Nanopipette Fabrication. For most BM-SICM experiments, nanopipettes (~90 nm radius at the opening, dimensions measured using a JEOL 2000FX transmission electron microscope (TEM)) were pulled from borosilicate glass capillaries (o.d. 1.2 mm, i.d. 0.69 mm, Harvard Apparatus) using a laser puller (P-2000, Sutter Instruments; pulling parameters: Line 1: Heat 330, Fil 3, Vel 30, Del 220, Pul -; Line 2: Heat 330, Fil 3, Vel 40, Del 180, Pul 120). For high-resolution scans of root hair cells, nanopipettes (~20 nm radius at the opening) were pulled from quartz capillaries (o.d. 1 mm, i.d 0.5 mm, Friedrich & Dimmock, pulling parameters: Line 1: Heat 750, Fil 4, Vel 30, Del 150, Pul 80; Line 2: Heat 650, Fil 3, Vel 40, Del 135, Pul 150). Typical TEM images of a borosilicate and of a quartz SICM probe, as used herein, are shown in Supporting Information, Figure S1.

Instrumentation. The SICM probe movement normal to the substrate was controlled using a piezoelectric positioning stage with a travel range of 38 μm (P-753-3CD, Physik Instrumente), while lateral movement of the substrate for XY positioning was achieved using a two-axis piezoelectric positioning system (Nano-BioS300, Mad City Laboratories, Inc.). A lock-in amplifier (SR830, Stanford Research Systems) was used to apply the oscillating bias in the BM-SICM setup and to extract the AC ion current amplitude and phase used for surface charge mapping and SICM feedback. The control of instrumentation and data collection was achieved using a custom written LabVIEW (2013, National Instruments) program through an FPGA card (NI PCIe-7852R, National Instruments) on the Warwick Electrochemical-Scanning Probe Microscopy platform.

Topographical and Surface Charge Mapping. The BM-SICM setup was built on the stage of an inverted optical microscope (Axiovert 40 CFL, Zeiss). To generate topographical and surface charge maps of the living cells, the probe was approached toward the surface at a rate of 500 nm s^{-1} for the lower resolution scans and 100 nm s^{-1} for the higher resolution root hair scan, while applying a small oscillation to the bias (10 mV rms amplitude, 270 Hz) about 0 V (so that SICM was a topographical probe)[54] until an increase in the AC phase signal was observed (0.5° for the lower resolution scans, 0.25° for high-resolution imaging with smaller nanopipettes). The vertical position of the piezoelectric actuator at this point was used to generate topographical maps of cells.[52] The tip potential was then linearly swept from 0 V to −0.4 V and then to 0.4 V and back to 0 V (all with respect to Ag/AgCl QRCE in solution bulk) at a rate of 800 mV s^{-1} and the AC phase and DC signal recorded for polarity-dependent surface charge mapping.[54] The tip was then retracted from the point of closest approach by a set distance (7 μm in the case of the root cells, 1 μm in the case of adipocyte cells) to prevent contact between the nanopipette and cell during the lateral movement as the probe was translated over the support-cell boundary, and the voltage sweep was again performed in order to obtain a bulk response for the normalization of ionic currents. The probe was then translated to the next pixel, and the sequence was repeated. This approach not only is powerful in revealing both surface charge and topography unambiguously but is also a pixel-level self-referencing technique enabling ultrasensitive surface charge measurements.

FEM Simulations. A 2D axisymmetric FEM simulation was performed in COMSOL Multiphysics (v4.4) using the transport of diluted species and electrostatics modules for a 90 nm radius glass nanopipette (geometrical arrangement of the probe determined from TEM) in both 10 mM KCl and 150 mM NaCl solution, which were the major components of the imaging media used for the root hair and adipocyte experiments, respectively. The tip was positioned at 30 nm (root hair) and 40 nm (adipocyte) above a substrate to which a varying surface charge density was applied (mimicking the experiments). A bias of ±0.4 V was applied to the nanopipette with respect to bulk. A surface charge of −1.125 mC m^{-2} was applied at the glass walls of a nanopipette probe, as used in previous work.[53−55,60] FEM simulations were also performed of a 40 nm diameter quartz nanopipette above a charged substrate in 10 mM electrolyte at a working distance of 15 nm to allow further quantification of the high-resolution root hair scan. For more details of the FEM model see Supporting Information.

RESULTS AND DISCUSSION

Principles of Surface Charge Mapping With a Nanopipette. The basic concept for independent mapping of the topography and surface charge of cells is illustrated in Figure 1.

DOI: 10.1021/jacs.5b13153
J. Am. Chem. Soc. 2016, 138, 3152−3160

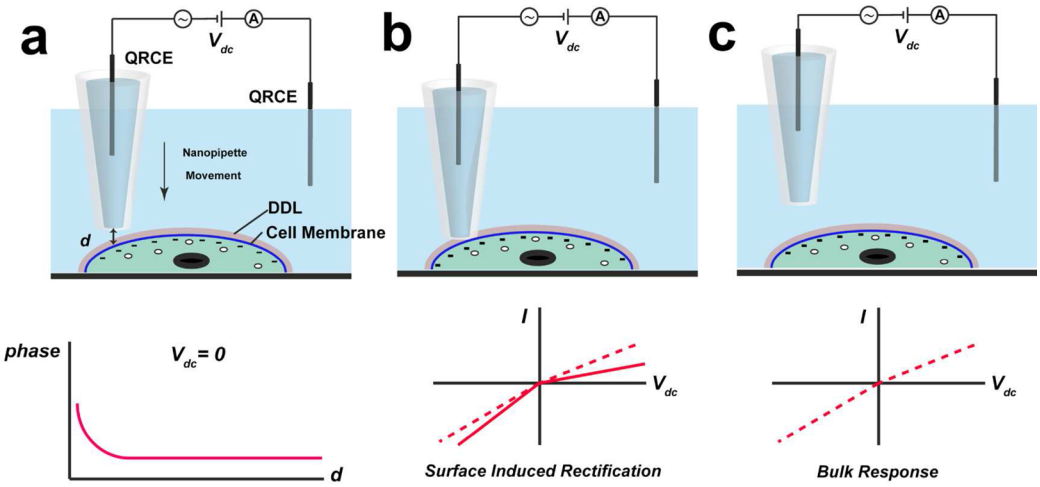

Figure 1. Schematic of the BM-SICM approach for noncovoluted surface charge/topographical imaging. A typical scan routine at each image pixel involves: (a) approaching the interface at 0 V net bias (V_{dc}) for determination of the topography with the AC phase due to the bias modulation used for accurate positioning (feedback) at tip to surface distance, d; (b) recording a voltammogram with the tip near the surface (distance defined by AC phase set point) by sweeping the pipette bias, V_{dc} (between the two QRCEs), and measuring the corresponding DC current, I, as indicated by the solid line; and (c) retracting the probe into bulk, followed by a voltammetric scan to obtain data for normalization of surface responses (dashed line).

The double layer at the surface has increasing effect on the nanopipette current at larger driving bias (V_{dc}), where SIR can considerably modify net ionic transport to and from the nanopipette.[54] In contrast, probe positioning is most accurate when surface charge effects are minimized, i.e., with no net nanopipette bias, where the effects of SIR are negligible.[54] Mapping of surface charge independently from topography can thus be performed by approaching the surface at 0 V net bias (using the AC phase signal from BM for feedback) to achieve a desired tip to surface distance, as shown on Figure 1a. A voltammogram is then run with the nanopipette situated at this desired position near the surface (Figure 1b). This response is compared with the current−voltage scan with the nanopipette in solution bulk (i.e., at distances larger than a few tip diameters, Figure 1c), in a self-referencing format at each pixel in an image.

Figure 2 depicts the principles of surface charge mapping using SICM. In bulk solutions, nanopipettes may exhibit an ion current rectification (ICR)[60−62] response depending on the charge and the opening size of a nanopipette with respect to the Debye length (which, in turn, depends on the ionic strength).[60,62] This arises because there is generally a cation-selective region (double layer) near the walls of the nanopipette, due to the negative surface charge at nanopipettes (glass or quartz) in aqueous solution, at neutral and higher pH,[63] coupled with asymmetric mass transport of ions from outside of the nanopipette (high mass transport rates due to hemispherical ion flow) and more restricted ion flow inside the nanopipette. As a result when a negative tip bias is applied with respect to bulk (Figure 2a), cations accumulate in the nanopipette as they enter the nanopipette at a faster rate than they can migrate up the nanopipette, resulting in a high-conductance state. Then, when the nanopipette is brought toward a negatively charged substrate (Figure 2b), the flux of cations to the nanopipette increases further because of the high-cation concentration in the diffuse double layer at the interface. This manifests as SIR and an enhanced current.[53,55] In the case where the nanopipette is brought toward a positively charged interface (Figure 2c), where there is an anion selective region, the migration of cations to the nanopipette opening is hindered, resulting in a smaller current magnitude at negative tip bias. When the tip bias is reversed (so that the tip electrode is positive with respect to the bulk), the mass transport scenario inverts, so that the more positive (less negative) the surface charge, the lower the resistance and the higher the current. The effect of the pipette conductance state on the AC response can be estimated using an RC circuit diagram, representing the pipette tip region, as shown in Figure 2d,e. As the conductance state of the pipet changes near the charged interface, the AC current through the capacitive element will either increase or decrease, with corresponding enhancement or reduction of the tip resistance, leading to variation of the AC phase shift toward 90° or 0°, respectively, depending on the surface charge.

FEM Simulations. FEM simulations (see details in Supporting Information), performed at the tip distances to be employed in the BM-SICM experiments and obtained with high accuracy from experimental approach curves at zero net bias,[52] allowed the generation of membrane charge-tip current characteristics (at the extreme CV potentials) for the quantitative estimation of the cell membrane surface charge for subsequent experiments. Simulations were run for both low- and high-electrolyte conditions (Figure 3a,b, respectively). It can be seen that in the low-electrolyte conditions, there is a much greater sensitivity to the surface charge of the substrate but that it is still possible, in media of high-ionic strength, to observe the effects of varying surface charge on the expected ionic current at both extreme tip polarities over the range of surface charges considered here, opening up the possibility of surface charge mapping under physiological conditions. The results of these simulations provide working curves for further estimation of surface charge magnitudes on the cellular membranes during imaging and establish a quantitative footing for the technique.

Mapping Charge at Root Hair Cells: Proof-of-Concept Measurements. To demonstrate the capabilities of BM-SICM to detect and map the surface charge of living cells, dynamic surface charge, and topographical, maps were first acquired on *Zea mays* root hairs (see optical micrograph on Figure 4a) in 10 mM KCl solution (pH 6.5). Root hair cell walls comprise primarily of cellulose microfibrils and other polysaccharides,

DOI: 10.1021/jacs.5b13153
J. Am. Chem. Soc. 2016, 138, 3152−3160

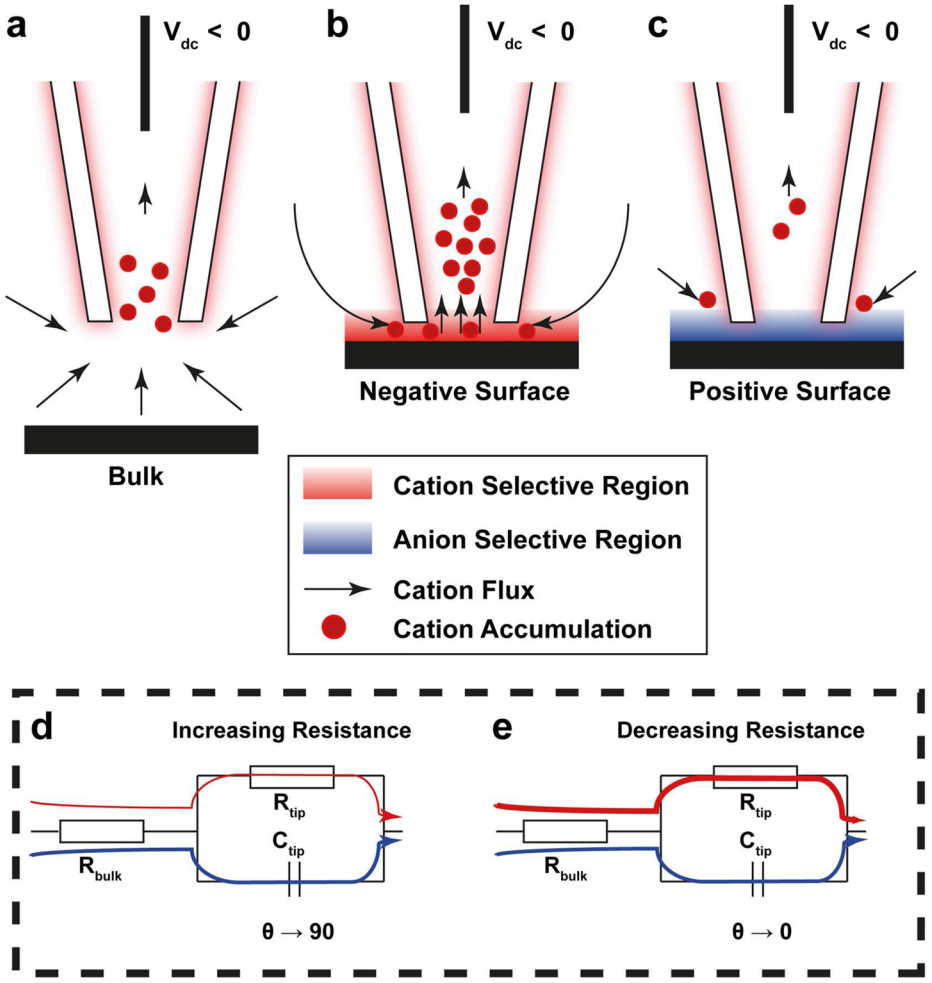

Figure 2. Cartoons (not to scale) demonstrating the charge distribution around a negatively charged nanopipette in bulk (a), near a negatively charged surface (b), and near a positively charged surface (c) and mass transport of cations (as an example) to the nanopipette with the internal solution biased negatively with respect to an exterior electrode. Circuit diagrams representing the nanopipette tip as an RC circuit for which there is a reduced current through the nanopipette opening when near a surface, (e.g., as compared to when in bulk) for which R_{tip} increases, resulting in a positive phase shift of AC currents, θ, toward 90°,[54] i.e., toward the ideal capacitative behavior (d) and when there is enhanced current through the end of the nanopipette opening (e.g., near a surface) so that R_{tip} decreases, resulting in a negative phase shift of AC current, θ, toward 0°, i.e., toward the ideal resistor behavior (e).

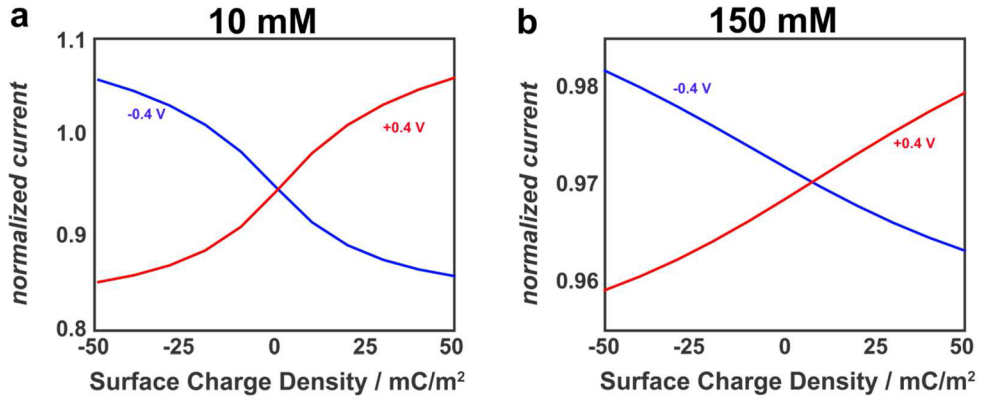

Figure 3. Working curve of normalized ionic current at a tip distance of (a) 30 nm above a charged interface in 10 mM electrolyte solution and (b) 40 nm above a charged interface in 150 mM electrolyte solution of varying surface charge density. The QRCE in the 90 nm radius pipette was biased +0.4 V (red) and −0.4 V (blue) with respect to that in bulk solution.

such as pectin,[64] and protect the root hair from pressure effects and maintain cell shape as well as acting as a filter, in which surface charge is expected to play an important role.[20] A typical topographical image of a root cell tip, extracted from the absolute values of vertical piezoelectric positioner extension, from a series of approaches, is shown in Figure 4b. Note that

DOI: 10.1021/jacs.5b13153
J. Am. Chem. Soc. 2016, 138, 3152−3160

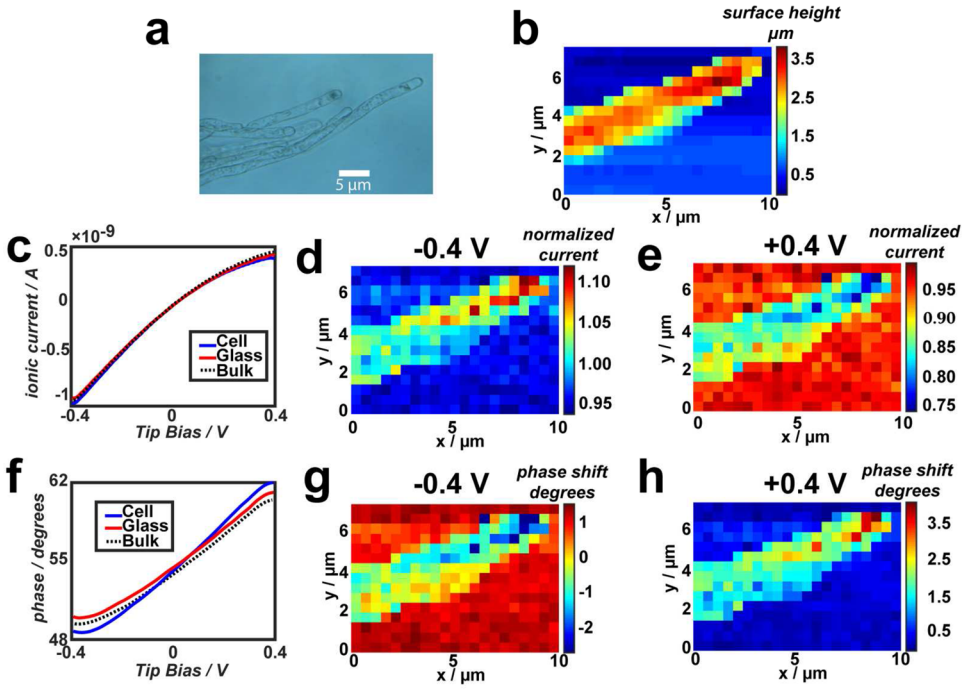

Figure 4. BM-SICM topographical and charge imaging on *Zea mays* root hair cells. (a) Optical microscope image of the cell sample on a glass slide substrate. (b) Recorded topographical image with a 90 nm-radius borosilicate nanopipette at 0 V mean bias and 10 mV harmonic oscillation at 270 Hz. The pixel pitch of the image is 500 nm, and there is no processing or interpolation of data. (c) Examples of acquired DC ionic current voltammograms near (tip 30 nm from) glass and cell surfaces (solid red and blue lines) compared to the response with the same nanopipette in bulk (dashed black line). Normalized (with respect to bulk values) DC ion current images at negative (d) and positive (e) tip biases. Corresponding AC phase voltammograms (f) and SICM images (g,h). The full dynamic image sequences of the DC currents and AC phase shifts, resolved by sweeping the potential at each image pixel, are shown in the form of video files ja5b13153_si_002.avi and ja5b13153_si_003.avi in the Supporting Information.

there is no interpolation or other postprocessing algorithms employed for these raw data. The lateral dimensions of the cell in this image correspond well with those from optical microscopy and reveal the cell height to be ca. 3 μm.

Typical nanopipette voltammetric responses, acquired during the image in Figure 3b with the probe near the cell, the glass substrate, and in bulk, are each compared in Figure 4c. It can be seen that the bulk current−voltage ($I-V$) response is typical of ICR of a negatively charged nanopipette with a higher conductance state (accumulation of cations at the nanopipette) at negative tip bias and a lower conductance state (expulsion of cations) at positive tip bias resulting in a diminished current.[54,55,60,62] There are differences between each of these voltammograms, which are magnified at the most extreme potentials (± 0.4 V). The $I-V$ response over the cell exhibits stronger (magnified) rectification compared with the nanopipette in bulk solution and near a glass surface, an effect that is diagnostic of more negative surface charge on the cell surface.

The measured responses at the extremes of the potential scan (−0.4 and 0.4 V tip bias), recorded at each pixel of the topographical image in Figure 4b, can be represented in a form of images, as shown in Figure 4d,e, respectively (the full dynamic frame sequence of 161 frames with a voltage step 0.01 V between frames is presented as a video file, ja5b13153_si_002.avi, in Supporting Information). Observations at negative tip bias (Figure 4d) evidence an enhanced current (with respect to bulk) above the root cell surface, which is indicative of the presence of a negative surface charge on the cell wall (as explained in Figure 2b),[20] most likely due to the presence of the polysaccharides, such as pectin. The glass surface at neutral pH also bears a slight negative charge caused by dissociation of silanol groups (point of zero charge at glass or silica in aqueous electrolytes is in pH range 2−4).[63]

The AC ion current components, and especially phase shift, offer higher sensitivity toward surface charge detection in comparison to measured DC currents. This is evident from the voltammetric data in Figure 4f, which show much more noticeable differences in the AC voltammetric phase response between the bulk solution, glass, and cell surfaces as compared to the DC data in Figure 4c. Furthermore, the AC phase images in Figure 4g,h reveal greater contrast and better signal/noise between the cell surface and glass support. The full set of AC phase voltammetric data is presented as a movie file ja5b13153_si_003.avi in the Supporting Information).

A particularly interesting charge feature can be observed in the region at the tip of the root hair (right-hand side top corner on images on Figure 4d,e and g,h), where the higher contrast (either larger change in the normalized current with respect to bulk or larger phase shift) indicates enhanced negative surface charge in this region. The negative surface charge of the cell helps regulate the exchange of cations across it and the exclusion of anions.[20] Ion-selective microelectrode measurements have shown that there is enhanced calcium flux to the tip of root hairs,[65] and our measurements indicate that the enhanced negative charge in this location may play a role in this relative enhancement of flux (in low−moderate electrolyte strengths).

It is important to consider whether there is any significant effect (or artifact) of the SICM tip on the ion distribution probed. For example, if the electric field at the nanopipette

DOI: 10.1021/jacs.5b13153
J. Am. Chem. Soc. 2016, 138, 3152−3160

induced the transport of cations across the cell membrane, then the effects seen would be magnified at negative tip potentials but not at positive potentials, and one would therefore observe a different apparent charge at the extreme positive and negative potentials, which is not the case in practice. The electric field at the pipette tip is not expected to induce any significant ionic transport through the cellular membrane, as the membrane resistance (10−100 GΩ)[66,67] is a few orders of magnitude higher than the resistance of the tip-to-substrate gap at the point of closest approach (of order of 10−100 MΩ), ensuring reliable topography and surface charge measurements.

Comparing the normalized current at the two extreme potentials presented in Figure 4 to the simulated working curves (Figure 3 a), one can estimate surface charge magnitudes on the cellular membrane (around −20 mC m^{-2} for the root hair) and the glass support (−3 mC m^{-2}). The surface charge estimate for the root hair is within the range of average values estimated in previous work on ensembles of cells using other techniques,[68] giving confidence in our new approach. The charged feature at the tip of the root hair, which has not been seen previously, has a much higher charge value of around −50 mC m^{-2}.[65]

Higher resolution BM-SICM images (1 × 1 μm area), acquired with a 40 nm diameter nanopipette on the tip region of the root cell (see Figure 5a), also evidenced significant surface charge heterogeneities at the cellular interface. Figure 5b depicts a typical normalized current map that was used for further quantification of charge magnitudes, aided by FEM simulations (details in Supporting Information). It can be seen from Figure 5c that the majority of the scanned region exhibited a surface charge of ca. −20 mC m^{-2}, similar to that observed in lower resolution images, but some regions of the high-resolution scan showed highly localized surface charges approaching −50 to −60 mC m^{-2}.

Surface Charge Mapping in Physiological Conditions. In many cases, the choice of medium for biological materials is rather limited, and many cell types need to be kept in physiological conditions (typically, electrolyte of high-ionic strength buffered to pH 7.2) to maintain an appropriate osmotic pressure and electrical potential across the cellular membrane. Unlike the plant cells studied above, AbSc cells do not exhibit a cell wall to protect the cell membrane from changes in osmotic pressure. As such, it is essential that they are maintained in media of ionic strength and composition similar to that of the extracellular conditions in which they would be present in the body; ionic strength of around 150 mM, containing predominantly NaCl (∼144 mM) as well as essential nutrients for cell growth, buffered to pH 7.2 (see Materials and Methods section).

While the ICR and SIR phenomena manifest most prominently at low-electrolyte concentrations, ICR has also been observed in electrolytes of high-ionic strength (100 mM and higher) if there is a sufficient charge on the nanopipette/nanopore walls and the probe opening size is sufficiently small.[62] It is therefore reasonable to expect that SIR would also be manifest under these conditions and that particular care would be needed when SICM experiments are performed over charged substrates, including cells, as topographical images could become convoluted with charge effects when using the classical SICM arrangement.[53]

We now explore whether BM-SICM can be used to probe the DDL, and hence surface charge, under physiological conditions, simultaneously with cell topography. Figure 6 shows typical results of SICM scans of an AbSc cell on a collagen support (26 × 26 pixels with pixel size of 200 nm), with an optical image of the scanned area presented in Figure 6a. These adipocyte cells were not fully matured and had a spindle shape, similar to that of preadipocyte cells.[69,70] As can be seen from the topographical data (Figure 6b), the section of the cell imaged appears as a reasonably flat structure of ∼2 μm width and around 1 μm in height. The DC current images (Figure 6c,d) and AC phase images (Figures 6f,g) at opposite polarities (± 0.4 V) demonstrate that there is a very clear contrast between the positively charged collagen substrate and the living AbSc cell (viability tested as explained in experimental section). Thus, at −0.4 V tip bias, the DC current is higher over the cell than over collagen, whereas the phase shift is greater (more positive) over collagen than over the cell. This contrast is inverted at positive tip bias (as expected, *vide supra*). However, the measured normalized DC

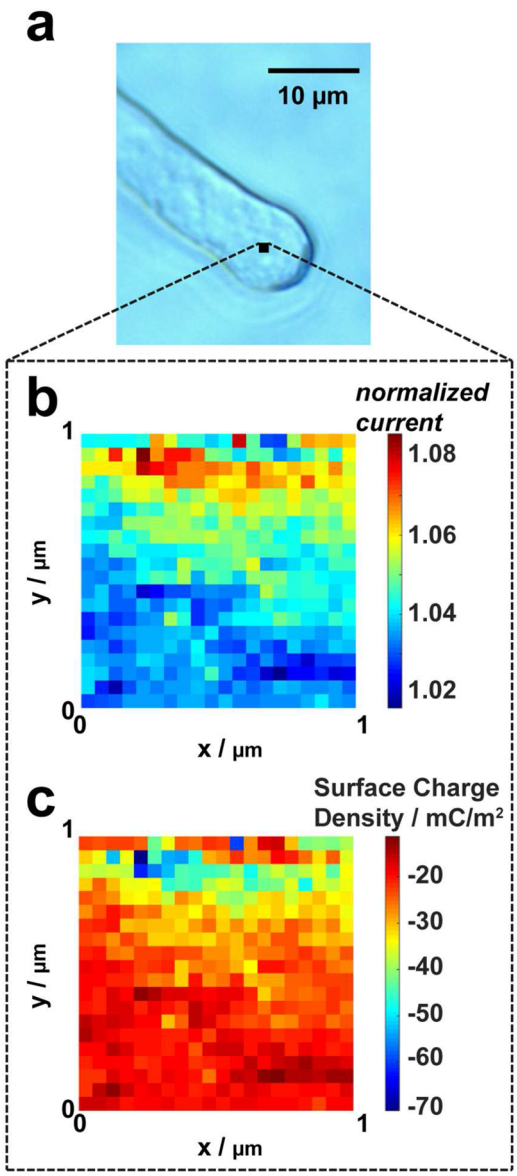

Figure 5. High-resolution surface charge map of a root hair tip with 50 nm pixel size. (a) An optical image of the scanned root hair with the scanned region represented by a black square; (b) normalized current at −0.4 V tip bias with respect to bulk; and (c) map of surface charge in the region scanned based on FEM simulations.

DOI: 10.1021/jacs.5b13153
J. Am. Chem. Soc. 2016, 138, 3152−3160

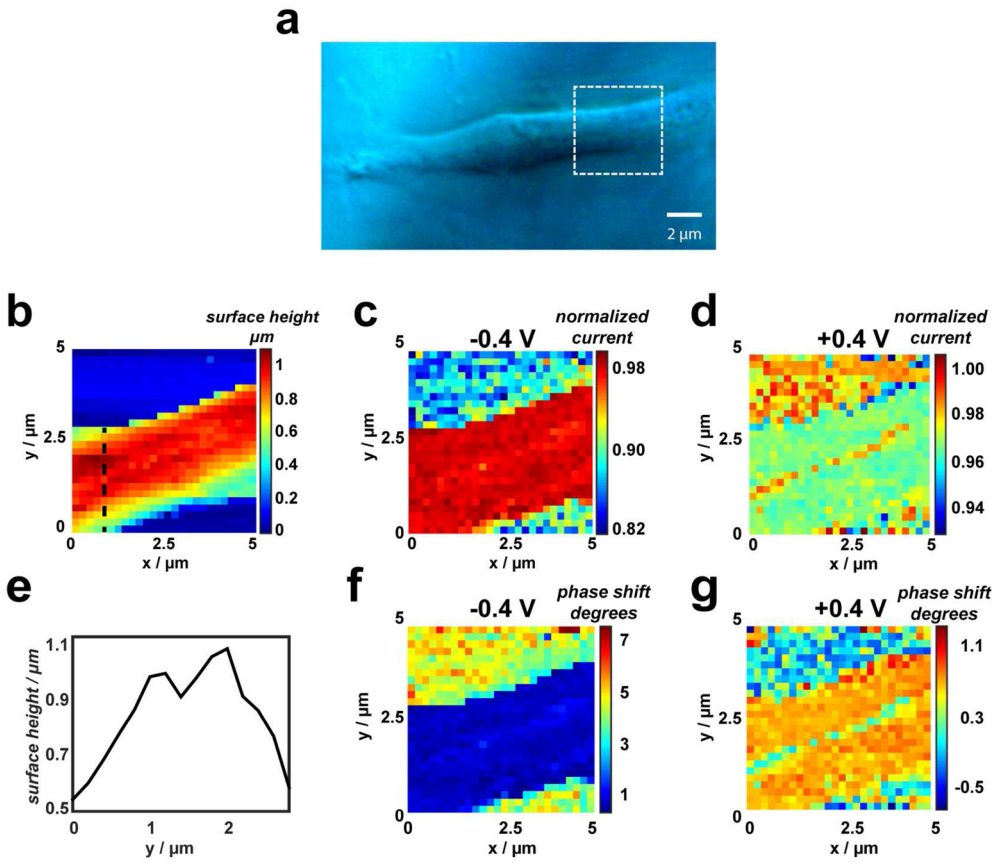

Figure 6. BM-SICM imaging of part of an adipocyte cell on a collagen support under physiological conditions (see text). (a) Optical microscope image of the spindle-shaped cell with the BM-SICM scan region indicated by white dashed lines. (b) Topographical map, containing 26 × 26 pixels and corresponding normalized (with respect to bulk responses) DC ion current images at (c) negative (−0.4 V) and (d) positive (0.4 V) tip biases. Line profile along the black dotted line in (b) shows the change in topography across the cell and reveals a trough feature in the cell surface morphology (e). AC phase data at (f) −0.4 V and (g) 0.4 V reveal a strong contrast between the cell and collagen support.

currents at both polarities do not exceed bulk values (i.e., normalized DC currents are all <1), in contrast to the behavior in low-electrolyte media (Figure 4). Moreover, at negative tip bias, the phase shift is always positive, but the magnitude is sensitive to the surface chemistry.

It is important to note that these data were collected using a relatively large tip diameter of around 180 nm. The effects we observe would become more significant with smaller tip diameters (closer tip−surface separations), relative to the size of the Debye length, but the clear observation that SIR effects are apparent under these conditions (moderate tip size and high-ionic strength) opens up considerable prospects for high-resolution SICM charge mapping experiments, as demonstrated previously for the root hair cells.

An interesting feature of the cell is a linear charge region along its length, which is evidenced at both tip polarities, but has a smaller contrast at negative bias. This charge heterogeneity extends along the central part of the cell, in a small topographical "valley" apparent from the line profile across the cell presented in Figure 6e. This charge feature is unlikely to be a topographical artifact as the width of the valley is larger than 2 tip diameters and is not observed on the side of the cell where the slope is similar in magnitude to the walls of the valley. Furthermore, this feature is observed regardless of the nanopipette probe polarity (see line profile, Supporting Information, Figure S3) and was seen in several scans of different AbSc cells, with a further example presented in the Supporting Information (Figure S4). As discussed below, this region is characterized by high positive charge and could pinpoint the location of key proteins in the cell membrane, which are considered to mediate fatty acid uptake and other functions.[71−73] The mechanism of free fatty acid transport is the subject of debate, and it has been suggested that it is mediated by a still to be identified membrane protein pump.[74] Other work indicates that fatty acid transporter proteins, which span the cell membrane, are characterized by the presence of the amino terminus on the extracellular side of the membrane.[75,76] This would result in a net positive charge, as observed in some regions of the AbSc cells.

For the AbSc cells in physiological conditions, comparison between theoretical and experimental results, at both positive and negative tip bias, suggests a cell surface charge of about −15 mC m^{-2} (Figure 3b), which is within the wide range of values quoted for other animal and plant cells, estimated using ensemble techniques.[68,77,78] The feature running along the center of the cell has a positive charge of approximately 50 mC m^{-2}.

As noted above, the simulations in 150 mM electrolyte strength predict that the normalized current would not exceed 1 for the cell membrane surface charge range and tip−surface distances considered, as is seen experimentally (Figure 6). In contrast, at low ionic strength (10 mM), the effects of surface charge are manifested more strongly in the SICM current response. Depending on the tip potential, the normalized

DOI: 10.1021/jacs.5b13153
J. Am. Chem. Soc. 2016, 138, 3152−3160

current is seen to result in current enhancements (or significantly diminished values) for high surface charges, as seen in the root hair data presented in Figure 4.

CONCLUSIONS

This work has demonstrated that SICM is a powerful probe for visualizing simultaneously both the topography and surface charge at living cells in both low electrolyte and in physiological media. This work thus adds major new capability to SICM, which already rivals AFM for high-resolution cell topography imaging. The possibility of probing cell surface charge under physiological conditions, where the double layer is compressed to small, subnanometer dimensions, is particularly noteworthy given that we employed relatively large pipette probes and tip/surface distances for much of the work. It has also been demonstrated that by reducing the size of the nanopipette opening employed, BM-SICM can become a tool for surface charge mapping with high spatial resolution. On the other hand, our work also raises some questions about the accuracy with which conventional SICM (with an applied bias) can be used to measure the true topography of cells, free from surface charge artifacts. The BM-SICM format that we describe neatly separates such effects by changing the applied bias and modulating the bias rather than the nanopipette position. This also provides a means of faster probe scanning at closer tip−substrate separations (higher spatial resolution).[79]

Our studies have highlighted the significant capabilities of BM-SICM for differentiating the surface charge of living cells from the support on which they are maintained, while also allowing for the identification of heterogeneities in charge across individual cells in the case of both root hair cells and AbSc cells, where new charge features have been observed, which enhance understanding of the functioning of these cells. Importantly, the technique described is quantitative and amenable to detailed finite element method analysis. Data can thus be analyzed to reveal surface charge values and 3D images of cell topography.

Ion conductance probes can be constructed with multiple channels,[80] and so in the future it may be possible to correlate surface charge with other properties, for example, by sampling the cell for subsequent off-line analysis[81] or by building spectroscopic functionality into SICM probes (e.g., tip enhanced Raman spectroscopy, near-field scanning optical microscopy, etc.).

ASSOCIATED CONTENT

Supporting Information

The Supporting Information is available free of charge on the ACS Publications website at DOI: 10.1021/jacs.5b13153.

FEM model details and a schematic as well as a TEM image of a typical probe; full image sequences from the DC ionic current and AC phase voltammogram data for the root hair cell data; normalized ionic current line profiles across the heterogeneously charged feature in the AbSc cell are presented (PDF)

Full dynamic image sequences of the DC currents (AVI)

Full dynamic image sequences of the AC phase shifts(AVI)

AUTHOR INFORMATION

Corresponding Author

*p.r.unwin@warwick.ac.uk

Notes

The authors declare no competing financial interest.

ACKNOWLEDGMENTS

This work was supported by the European Research Council through Project ERC-2009 AdG 247143-QUANTIF (P.R.U. and B.P.N.), the EPSRC through the MOAC DTC, grant no. EP/F500378/1 (D.P. and A.P.), a Marie Curie IntraEuropean Fellowship 626158 FUNICIS (D.M.), and the BBSRC (P.D.V.).

REFERENCES

(1) Trefalt, G.; Behrens, S. H.; Borkovec, M. *Langmuir* **2016**, *32*, 380.
(2) Han, Y.; Wang, X.; Dai, H.; Li, S. *ACS Appl. Mater. Interfaces* **2012**, *4*, 4616.
(3) Oncsik, T.; Trefalt, G.; Csendes, Z.; Szilagyi, I.; Borkovec, M. *Langmuir* **2014**, *30*, 733.
(4) Hellevang, H.; Miri, R.; Haile, B. G. *Cryst. Growth Des.* **2014**, *14*, 6451.
(5) Yanina, S. V.; Rosso, K. M. *Science* **2008**, *320*, 218.
(6) Lan, W.-J.; Holden, D. A.; White, H. S. *J. Am. Chem. Soc.* **2011**, *133*, 13300.
(7) Guo, W.; Tian, Y.; Jiang, L. *Acc. Chem. Res.* **2013**, *46*, 2834.
(8) Armstrong, J. A.; Bernal, E. E. L. n.; Yaroshchuk, A.; Bruening, M. L. *Langmuir* **2013**, *29*, 10287.
(9) Cong, X.; Poyton, M. F.; Baxter, A. J.; Pullanchery, S.; Cremer, P. S. *J. Am. Chem. Soc.* **2015**, *137*, 7785.
(10) Asati, A.; Santra, S.; Kaittanis, C.; Perez, J. M. *ACS Nano* **2010**, *4*, 5321.
(11) Ghosh, P. S.; Kim, C.-K.; Han, G.; Forbes, N. S.; Rotello, V. M. *ACS Nano* **2008**, *2*, 2213.
(12) Zenobi, R. *Science* **2013**, *342*, 1243259.
(13) Lesniak, A.; Salvati, A.; Santos-Martinez, M. J.; Radomski, M. W.; Dawson, K. A.; Åberg, C. *J. Am. Chem. Soc.* **2013**, *135*, 1438.
(14) Lee, K.-D.; Hong, K.; Papahadjopoulos, D. *Biochim. Biophys. Acta, Biomembr.* **1992**, *1103*, 185.
(15) Christianson, H. C.; Svensson, K. J.; van Kuppevelt, T. H.; Li, J.-P.; Belting, M. *Proc. Natl. Acad. Sci. U. S. A.* **2013**, *110*, 17380.
(16) Shi, X.; Bi, Y.; Yang, W.; Guo, X.; Jiang, Y.; Wan, C.; Li, L.; Bai, Y.; Guo, J.; Wang, Y. *Nature* **2013**, *493*, 111.
(17) Bakhti, M.; Snaidero, N.; Schneider, D.; Aggarwal, S.; Möbius, W.; Janshoff, A.; Eckhardt, M.; Nave, K.-A.; Simons, M. *Proc. Natl. Acad. Sci. U. S. A.* **2013**, *110*, 3143.
(18) Busscher, H. J.; van der Mei, H. C. *PLoS Pathog.* **2012**, *8*, e1002440.
(19) Dubiel, E. A.; Martin, Y.; Vermette, P. *Chem. Rev.* **2011**, *111*, 2900.
(20) Gregory, P. J. *Plant roots: growth, activity and interactions with the soil*; John Wiley & Sons: Hoboken, NJ, 2008.
(21) Tedja, R.; Lim, M.; Amal, R.; Marquis, C. *ACS Nano* **2012**, *6*, 4083.
(22) Barisik, M.; Atalay, S.; Beskok, A.; Qian, S. *J. Phys. Chem. C* **2014**, *118*, 1836.
(23) Kim, S. T.; Saha, K.; Kim, C.; Rotello, V. M. *Acc. Chem. Res.* **2013**, *46*, 681.
(24) Rivera-Gil, P.; Jimenez De Aberasturi, D.; Wulf, V.; Pelaz, B.; Del Pino, P.; Zhao, Y.; De La Fuente, J. M.; Ruiz De Larramendi, I.; Rojo, T.; Liang, X.-J. *Acc. Chem. Res.* **2012**, *46*, 743.
(25) Haupt, A.; Campetelli, A.; Bonazzi, D.; Piel, M.; Chang, F.; Minc, N. *PLoS Biol.* **2014**, *12*, e1002029.
(26) Wong, J. Y.; Langer, R.; Ingber, D. E. *Proc. Natl. Acad. Sci. U. S. A.* **1994**, *91*, 3201.
(27) Klenerman, D.; Korchev, Y. E.; Davis, S. J. *Curr. Opin. Chem. Biol.* **2011**, *15*, 696.
(28) Bard, A. J.; Faulkner, L. R. *Electrochemical methods: fundamentals and applications*; Wiley: New York, 1980; Vol. 2.
(29) Henderson, E.; Haydon, P.; Sakaguchi, D. *Science* **1992**, *257*, 1944.

DOI: 10.1021/jacs.5b13153
J. Am. Chem. Soc. 2016, 138, 3152−3160

(30) Dammer, U.; Popescu, O.; Wagner, P.; Anselmetti, D.; Guntherodt, H.-J.; Misevic, G. N. *Science* **1995**, *267*, 1173.
(31) Raman, A.; Trigueros, S.; Cartagena, A.; Stevenson, A.; Susilo, M.; Nauman, E.; Contera, S. A. *Nat. Nanotechnol.* **2011**, *6*, 809.
(32) Müller, D. J.; Dufrêne, Y. F. *Trends Cell Biol.* **2011**, *21*, 461.
(33) Alsteens, D.; Dupres, V.; Yunus, S.; Latgé, J.-P.; Heinisch, J. r. J.; Dufrêne, Y. F. *Langmuir* **2012**, *28*, 16738.
(34) Hillier, A. C.; Kim, S.; Bard, A. J. *J. Phys. Chem.* **1996**, *100*, 18808.
(35) Miyatani, T.; Horii, M.; Rosa, A.; Fujihira, M.; Marti, O. *Appl. Phys. Lett.* **1997**, *71*, 2632.
(36) Miyatani, T.; Okamoto, S.; Rosa, A.; Marti, O.; Fujihira, M. *Appl. Phys. A: Mater. Sci. Process.* **1998**, *66*, S349.
(37) Manne, S.; Cleveland, J.; Gaub, H.; Stucky, G.; Hansma, P. *Langmuir* **1994**, *10*, 4409.
(38) Xu, S.; Arnsdorf, M. F. *Proc. Natl. Acad. Sci. U. S. A.* **1995**, *92*, 10384.
(39) Ahimou, F.; Denis, F. A.; Touhami, A.; Dufrêne, Y. F. *Langmuir* **2002**, *18*, 9937.
(40) Almonte, L.; Lopez-Elvira, E.; Baró, A. M. *ChemPhysChem* **2014**, *15*, 2768.
(41) Sotres, J.; Baró, A. *Appl. Phys. Lett.* **2008**, *93*, 103903.
(42) Sotres, J.; Baró, A. *Biophys. J.* **2010**, *98*, 1995.
(43) Korchev, Y.; Milovanovic, M.; Bashford, C.; Bennett, D.; Sviderskaya, E.; Vodyanoy, I.; Lab, M. *J. Microsc.* **1997**, *188*, 17.
(44) Shevchuk, A. I.; Frolenkov, G. I.; Sánchez, D.; James, P. S.; Freedman, N.; Lab, M. J.; Jones, R.; Klenerman, D.; Korchev, Y. E. *Angew. Chem.* **2006**, *118*, 2270.
(45) Happel, P.; Thatenhorst, D.; Dietzel, I. D. *Sensors* **2012**, *12*, 14983.
(46) Rheinlaender, J.; Schaffer, T. E. *Soft Matter* **2013**, *9*, 3230.
(47) Hansma, P.; Drake, B.; Marti, O.; Gould, S.; Prater, C. *Science* **1989**, *243*, 641.
(48) Chen, C. C.; Zhou, Y.; Baker, L. A. *Annu. Rev. Anal. Chem.* **2012**, *5*, 207.
(49) Takahashi, Y.; Murakami, Y.; Nagamine, K.; Shiku, H.; Aoyagi, S.; Yasukawa, T.; Kanzaki, M.; Matsue, T. *Phys. Chem. Chem. Phys.* **2010**, *12*, 10012.
(50) Takahashi, Y.; Ito, K.; Wang, X.; Matsumae, Y.; Komaki, H.; Kumatani, A.; Ino, K.; Shiku, H.; Matsue, T. *Electrochemistry* **2014**, *82*, 331.
(51) Shevchuk, A. I.; Gorelik, J.; Harding, S. E.; Lab, M. J.; Klenerman, D.; Korchev, Y. E. *Biophys. J.* **2001**, *81*, 1759.
(52) McKelvey, K.; Perry, D.; Byers, J. C.; Colburn, A. W.; Unwin, P. R. *Anal. Chem.* **2014**, *86*, 3639.
(53) McKelvey, K.; Kinnear, S. L.; Perry, D.; Momotenko, D.; Unwin, P. R. *J. Am. Chem. Soc.* **2014**, *136*, 13735.
(54) Perry, D.; Al Botros, R.; Momotenko, D.; Kinnear, S. L.; Unwin, P. R. *ACS Nano* **2015**, *9*, 7266.
(55) Sa, N.; Lan, W.-J.; Shi, W.; Baker, L. A. *ACS Nano* **2013**, *7*, 11272.
(56) Clarke, R. W.; Zhukov, A.; Richards, O.; Johnson, N.; Ostanin, V.; Klenerman, D. *J. Am. Chem. Soc.* **2013**, *135*, 322.
(57) Gilroy, S.; Jones, D. L. *Trends Plant Sci.* **2000**, *5*, 56.
(58) Chung, T.-H.; Wu, S.-H.; Yao, M.; Lu, C.-W.; Lin, Y.-S.; Hung, Y.; Mou, C.-Y.; Chen, Y.-C.; Huang, D.-M. *Biomaterials* **2007**, *28*, 2959.
(59) Strober, W. *Curr. Protoc. Immunol.* **2001**, *3B*, 1.
(60) Momotenko, D.; Cortes-Salazar, F.; Josserand, J.; Liu, S.; Shao, Y.; Girault, H. H. *Phys. Chem. Chem. Phys.* **2011**, *13*, 5430.
(61) Siwy, Z.; Heins, E.; Harrell, C. C.; Kohli, P.; Martin, C. R. *J. Am. Chem. Soc.* **2004**, *126*, 10850.
(62) White, H. S.; Bund, A. *Langmuir* **2008**, *24*, 2212.
(63) Behrens, S. H.; Grier, D. G. *J. Chem. Phys.* **2001**, *115*, 6716.
(64) Showalter, A. M. *Plant Cell* **1993**, *5*, 9.
(65) Jones, D. L.; Shaff, J. E.; Kochian, L. V. *Planta* **1995**, *197*, 672.
(66) Sakmann, B.; Neher, E. *Annu. Rev. Physiol.* **1984**, *46*, 455.
(67) Jonas, E. A.; Knox, R. J.; Kaczmarek, L. K. *Neuron* **1997**, *19*, 7.
(68) Kinraide, T. B.; Wang, P. *J. Exp. Bot.* **2010**, *61*, 2507.
(69) Daya, S.; Loughlin, A. J.; MacQueen, H. A. *Differentiation* **2007**, *75*, 360.
(70) Hemmrich, K.; Von Heimburg, D.; Cierpka, K.; Haydarlioglu, S.; Pallua, N. *Differentiation* **2005**, *73*, 28.
(71) Harmon, C. M.; Abumrad, N. A. *J. Membr. Biol.* **1993**, *133*, 43.
(72) Abumrad, N. A.; El-Maghrabi, M. R.; Amri, E.; Lopez, E.; Grimaldi, P. *J. Biol. Chem.* **1993**, *268*, 17665.
(73) Schneider, H.; Staudacher, S.; Poppelreuther, M.; Stremmel, W.; Ehehalt, R.; Füllekrug, J. *Arch. Biochem. Biophys.* **2014**, *546*, 8.
(74) Kampf, J. P.; Parmley, D.; Kleinfeld, A. M. *Am. J. Physiol. Endocrind. Metab.* **2007**, *293*, E1207.
(75) Lewis, S. E.; Listenberger, L. L.; Ory, D. S.; Schaffer, J. E. *J. Biol. Chem.* **2001**, *276*, 37042.
(76) Stahl, A. *Pfluegers Arch.* **2004**, *447*, 722.
(77) Rubenstein, D.; Yin, W.; Frame, M. D. *Biofluid Mechanics: An Introduction to Fluid Mechanics, Macrocirculation, and Microcirculation*; Academic Press: Waltham, MA, 2011.
(78) Neu, B.; Meiselman, H. J. *Biophys. J.* **2002**, *83*, 2482.
(79) Rheinlaender, J.; Geisse, N. A.; Proksch, R.; Schäffer, T. E. *Langmuir* **2011**, *27*, 697.
(80) Paulose Nadappuram, B.; McKelvey, K.; Byers, J. C.; Güell, A. G.; Colburn, A. W.; Lazenby, R. A.; Unwin, P. R. *Anal. Chem.* **2015**, *87*, 3566.
(81) Actis, P.; Maalouf, M. M.; Kim, H. J.; Lohith, A.; Vilozny, B.; Seger, R. A.; Pourmand, N. *ACS Nano* **2014**, *8*, 546.

DOI: 10.1021/jacs.5b13153
J. Am. Chem. Soc. 2016, 138, 3152−3160